Atmos. Chem. Phys. Discuss., 9, 7781–7823, 2009
www.atmos-chem-phys-discuss.net/9/7781/2009/

Atmospheric Chemistry and Physics Discussions

This discussion paper is/has been under review for the journal *Atmospheric Chemistry and Physics (ACP)*. Please refer to the corresponding final paper in *ACP* if available.

Physical properties of High Arctic tropospheric particles during winter

L. Bourdages[1], T. J. Duck[1], G. Lesins[1], J. R. Drummond[1], and E. W. Eloranta[2]

[1]Department of Physics and Atmospheric Science, Dalhousie University, Halifax, Canada
[2]Space Science and Engineering Center, University of Wisconsin, Madison, USA

Received: 11 March 2009 – Accepted: 14 March 2009 – Published: 24 March 2009

Correspondence to: T. J. Duck (tom.duck@dal.ca)

Published by Copernicus Publications on behalf of the European Geosciences Union.

Abstract

A climatology of particle properties in the wintertime High Arctic troposphere is constructed using measurements from a lidar and cloud radar located at Eureka, Nunavut Territory (80° N, 86° W). Four different particle groupings are considered: aerosols, mixed-phase clouds, ice clouds and boundary-layer ice crystals. Two-dimensional histograms of occurrence probabilities against depolarization and radar/lidar colour ratio, as well as their vertical distributions, are presented. The largest ice crystals originate from mixed-phase clouds, whereas the smallest are topographic blowing snow residuals in the boundary layer. Ice cloud crystals have depolarization and size decreasing with height. The depolarization trend is associated with the large ice crystal sub-population. Small crystals depolarize more than large ones in ice clouds at a given altitude, and show constant modal depolarization with height. Ice clouds in the mid-troposphere are sometimes observed to precipitate to the ground. Water clouds are constrained to the lower troposphere and are associated with the surface inversion layer depth. Aerosols are most abundant near the ground and are frequently mixed with the other particle types. The data are used to construct a classification chart for particle scattering in wintertime Arctic conditions.

1 Introduction

A persistent thermal inversion is observed in the Arctic lower troposphere during winter, with average temperatures increasing 10 K in the first kilometer from ground (Curry et al., 1996; Lesins et al., 2009b). The inversion is caused by radiative cooling of surface ice and snow. Clear-sky simulations indicate that surface temperatures should drop below 230 K when air is five days removed from the maritime polar environment, and continue to cool thereafter (Curry, 1983). Since the surface is typically warmer than that (e.g., Lesins et al., 2009b), a counter-balancing infrared forcing from atmospheric particles, including clouds, is presumed.

Early studies proposed a role for "diamond dust" ice crystals that nucleate in the very cold conditions found at high latitudes during winter, but subsequent measurements showed they have a negligible impact (Intrieri and Shupe, 2004). Ice precipitation from thin water clouds can be mistaken for diamond dust (Intrieri and Shupe, 2004), as can residual blowing snow lofted from mountainous terrain (Lesins et al., 2009a). Clouds in general play a major role in the radiative transfer (Curry et al., 1996). Aerosols, on the other hand, have a small impact on scattering and visibility (Hoff, 1988; Trivett et al., 1988; Leaitch et al., 1989), but may promote dehydration and so provide a negative surface forcing (Blanchet and Girard, 1995). Cooling in the 20 micron "dirty" window of the water vapor spectrum is greater in the Arctic than at midlatitudes due to the cold dry conditions (Curry et al., 1996), and so any changes in forcing may be accompanied by a strong water vapour feedback. The relative contribution from each forcing mechanism and the relationship to lower-tropospheric thermal structure is uncertain, but is important to know given the impact of radiative transfer and surface temperatures on the stability of Arctic sea ice and the climate system in general (Curry et al., 1993).

Arctic tropospheric particles and the processes that govern them are poorly understood due to the inherent difficulties in conducting research and observational campaigns at high latitudes, especially during winter. The harsh environment imposes substantial costs and limits on accessibility which leads to scarce and isolated data sets. Research is further complicated by the facts that visual observations have known deficiencies in dark wintertime conditions (Intrieri and Shupe, 2004) and that passive satellite sensors have difficulties distinguishing clouds and particles in the inversion layer from the colder surface below (Curry et al., 1996).

Several campaigns have been conducted to measure Arctic particle optical, macro- and microphysical characteristics: the Canadian Arctic Haze Study and Arctic Gas and Air Sampling Program (AGASP; see Leaitch et al., 1989 and references therein), the FIRE Arctic Clouds Experiment (FIRE-ACE; Curry et al., 2000), the Surface Heat Budget of the Arctic Ocean campaign (SHEBA; Uttal et al., 2002), and the Mixed-Phase Arctic Cloud Experiment (MPACE; Verlinde et al., 2007). Such activities are

most often conducted during the spring and summer and are typically of short duration, rarely longer than a few months to a year. Multi-year statistical data sets are needed, particularly for particle sizes, shapes and phases, which are directly related to radiative properties (Curry et al., 2000). Of the aircraft campaigns listed above, not one was conducted during the winter months, and this represents a substantial observational gap which the present study helps to address.

The Canadian Network for the Detection of Atmospheric Change (CANDAC) established the Polar Environment Atmospheric Research Laboratory (PEARL) at Eureka, Nunavut Territory (80° N, 86° W) in collaboration with Environment Canada (EC) for year-round measurements of the atmosphere from the surface to 100 km altitude. PEARL is co-located with the Eureka Weather Station on Ellesmere Island (Fig. 1), and is the most northern permanent civilian research facility in Canada. A comprehensive set of remote-sensing and in-situ instruments was installed by CANDAC and the National Oceanic and Atmospheric Association (NOAA) Study of Environmental Arctic Change (SEARCH) program. Measurements are being collected on an ongoing basis.

In this study, atmospheric particles observed above Eureka during three winters from 2005 to 2008 are characterized according to their scattering properties. Section 2 describes the active remote sensors used: a High Spectral Resolution Lidar and a Millimeter-wave Cloud Radar. Section 3 divides the particles into categories and provides the characterization methodology. An illustrative example is given to motivate a statistical approach. Results are presented in Sect. 4, and are discussed in Sect. 5. Mie scattering theory is used to estimate particle effective radii, and the distributions of particle sizes, altitude ranges, and depolarization values are reviewed and compared with other measurements. Section 6 summarizes the results and discusses future research possibilities.

2 Instrumentation

2.1 The Zero-altitude PEARL Auxiliary Laboratory

The measurements were obtained at the Zero-altitude PEARL Axillary Laboratory (ØPAL), which is co-located with the Eureka Weather Station at 10 m elevation above sea level. Table 1 lists the ØPAL instruments and their respective capabilities.

Figure 2 shows ØPAL and highlights the two instruments of interest here: the Arctic High Spectral Resolution Lidar (AHSRL) and the Millimeter-wave Cloud Radar (MMCR). The instruments are housed in climate-controlled shipping containers which are powered by a diesel generating station that is 215 m to the south. The measurements from each instrument are transmitted from Eureka by satellite link, and are archived by CANDAC. Data from both the AHSRL and MMCR can be accessed through the University of Wisconsin's lidar group web site: http://lidar.ssec.wisc.edu/.

2.2 Arctic High Spectral Resolution Lidar

The Arctic High Spectral Resolution Lidar (AHSRL) was developed at the University of Wisconsin and is supported at PEARL by NOAA's SEARCH program. It has collected quasi-continuous data at Eureka from August 2005 to present, with occasional down time due to maintenance requirements. The instrument is an Internet appliance designed for unattended operation. Technical specifications for the AHSRL are presented in Table 2.

The transmitter consists of a frequency-doubled diode-pumped Nd:YAG laser emitting at a 4 kHz repetition rate and 532 nm wavelength. The laser is seeded and locked using an iodine vapour cell so that the frequency of the light is stable and the line width is narrow. The outgoing beam is circularly polarized and is transmitted at a 4° zenith angle to avoid specular reflections from horizontally-oriented ice crystals. A 40 cm telescope is used by both the transmitter and receiver. The receiver's 45 µrad field of view significantly reduces the background light level and contributions from

multiple scattering. Incoming photons are separated according to polarization state, and are filtered using a 0.35-nm bandpass interference filter and a 8-GHz bandpass pressure-tuned etalon. Signal detection is performed using Geiger-mode avalanche photodiodes and photon-counting electronics. Additional technical details are given by Razenkov et al. (2002).

The lidar measures the particle backscatter cross-section and depolarization ratio. The depolarization may be used to differentiate between spherical liquid droplets and crystalline particles, which have low and high depolarization values, respectively (e.g., see Intrieri and Shupe, 2004). Appropriate thresholds for the interpretation are established in this study.

The AHSRL data employs 2.5 s temporal and 7.5 m spatial resolutions and can measure volume backscatter cross-section profiles up to an optical depth of approximately 4, beyond which the transmitted beam is too attenuated. In this work, 30 s and 15 m averaged measurements are used. The standard deviation for each average (determined from the intrinsic resolution data) is employed to filter out data with excessive atmospheric variability or noise.

2.3 CANDAC Millimeter-Wave Cloud Radar

CANDAC's Millimeter-wave Cloud Radar (MMCR) is co-located with the AHSRL. This type of radar is effective for cloud microphysics studies because it combines high sensitivity and high spatial resolution. With a wavelength of 8.6 mm, the scattering from atmospheric particles is in the Rayleigh regime and thus has a strong dependence on the particle size.

Compared to wind profiling and precipitation surveillance radars (wavelengths from 3 to 600 cm), millimeter wavelength radars have the advantage of increased sensitivity to smaller particles, but the disadvantage of strong attenuation from rainfall. This disadvantage is not relevant during the cold High Arctic winter since the only precipitation is frozen. Snowfall and ice crystals attenuate the radar signal minimally. Water vapor also has negligible impact since the wintertime Arctic atmosphere is relatively dry.

The MMCR has been collecting data since August 2005 and is designed for remote operation with an intended lifetime of at least 10 years. It provides information on Doppler velocity, spectral width and radar reflectivity. The latter can be related to the backscattering cross-section of the atmospheric particles, which allows direct comparison with the AHSRL backscatter measurements.

Technical specifications for the MMCR are given in Table 3. The general setup of the system is similar to that of the lidar with a coaxial, vertically pointing transmitter and receiver. The instrument employs a frequency converter which produces 34.86 GHz microwaves from the internal 60 MHz-frequency waveforms. Pulses are emitted vertically by a 2 m diameter high-gain antenna. The antenna also acts as the receiving apparatus. The measured return signal is converted to 60 MHz frequency and analyzed by a commercial data system from NOAA. Doppler velocities and reflectivity/backscatter cross-sections are retrieved.

The millimeter-wave pulses can be compressed to improve the instrument's sensitivity and power. This has the disadvantage of creating sidelobe artifacts, especially in regions where reflectivity is strong. In order to get the best data product possible, the MMCR cycles through four signal acquisition modes with different pulse width and pulse-encoding. Combination of these modes allows for optimization of the signal through increased sensitivity while accounting for the artifacts. Details are given by Moran et al. (1998).

The MMCR measures reflectivity from 90 m to 20 km in altitude, and is sensitive to volume backscatter cross-sections greater than 10^{-14} $m^{-1}sr^{-1}$. Data are recorded with a temporal and spatial resolution of 10 s and 90 m, respectively. For the purposes of this study, the data are interpolated to the same resolutions used by the averaged lidar measurements (30 s and 15 m).

3 Methodology

A statistical approach can be motivated with an example. Figure 3 shows the typical wintertime scattering features observed at Eureka in a single 24 h measurement on 4–5 March 2007. From 14:00 to 24:00 UTC, ice crystals (high backscatter, high depolarization) were detected in the lowest 0.5 km by both the radar and the lidar. Ice clouds (high backscatter, high depolarization) were present in the middle troposphere from approximately 16:00 to 08:00 UTC, and ended by precipitating to the surface. These cirrus-like clouds occur in the same temperature range (approximately 210–250 K) found in the upper half of the midlatitude troposphere. An aerosol event (low backscatter, low depolarization) between 1 and 4 km altitude began at 03:00 UTC. Note that the aerosol event was largely unseen by the radar. A mixed-phase cloud appeared within the aerosol layer at approximately 10:00 UTC and persisted through the end of the measurement. "Mixed-phase" is the term used to describe a geometrically thin water cloud with ice precipitation below. The water component is identified by enhanced lidar backscatter with low depolarization, whereas the ice precipitate has high depolarization. The altitude of the thin water cloud corresponds to the top of the inversion layer as measured by the 12:00 UTC radiosonde (not shown). Ice clouds were seen again above 4 km from 09:00 to 14:00 UTC. Noise is evident at the upper altitudes in the depolarzation ratio measurement between 23:00 and 03:00 UTC, and to a lesser extent in the lidar backscatter. Such noise is removed from further analysis by a filtering process described later.

The radar and lidar measure the particle volume backscatter cross-section (β), which is related to the backscatter cross-section $\sigma_\pi(r)$ and number density $n(r)$ of particles with radius r by

$$\beta = \int_0^\infty \sigma_\pi n dr.$$

The mean particle cross section $\overline{\sigma}_\pi$ is defined by

$$\overline{\sigma}_\pi = \frac{\int_0^\infty \sigma_\pi n dr}{\int_0^\infty n dr}$$

and the total number of particles N is

$$N = \int_0^\infty n dr.$$

Thus, the volume backscatter cross-section can be re-written as

$$\beta = N\overline{\sigma}_\pi$$

The backscatter cross-section depends on wavelength and so is different for the lidar and the radar. Taking the ratio between the two backscatter cross-sections gives

$$\frac{\beta_{\text{radar}}}{\beta_{\text{lidar}}} = \frac{N\overline{\sigma}_\pi(\lambda_{\text{radar}})}{N\overline{\sigma}_\pi(\lambda_{\text{lidar}})} = \frac{\overline{\sigma}_\pi(\lambda_{\text{radar}})}{\overline{\sigma}_\pi(\lambda_{\text{lidar}})} \quad , \tag{1}$$

which removes the dependence on number density and so allows for a deeper analysis of particle physical properties. More precisely, the backscatter cross-section ratio – hereafter referred to as the colour ratio – described by Eq. (1) is a proxy for particle size. This relationship is explored in Sect. 5.2.

Practical application of Eq. (1) requires that β_{radar} and β_{lidar} exceed the minimum thresholds of detection for each instrument. Figure 3 demonstrates that this requirement is not satisfied for aerosols, which are generally invisible to the radar. The radar's insensitivity to very small particles follows from Fig. 3b, which shows a maximum lidar volume backscatter cross-section for aerosols is 10^{-5} m^{-1}sr^{-1}. Using Mie theory (see Sect. 5.2), the colour ratio for the sub-micron particles in Arctic haze (e.g., Leaitch et al., 1989) is about 10^{-12}, leading to an expected radar volume backscatter cross-section of 10^{-17} m^{-1} sr^{-1}. This is three orders of magnitude less than the edge of detectability by the radar. In other words, the aerosol cloud concentrations would need to be

at least 1000 times greater than the maximum observed under normal circumstances to be seen by the radar. Since aerosol particles cannot be detected with both instruments, an interpretation in terms of particle size is not possible. Aerosols will, however, continue to be considered in terms of optical scattering properties and their potential for mixing with other scatterer types. Note that although there are similar detectability issues for polar cloud particles with the CloudSat radar and CALIPSO lidar satellite instruments (e.g., Grenier et al., 2009), Fig. 3 suggests that is not the case here.

Figure 4 shows the colour ratio for the measurement given in Fig. 3. The colour ratio measurement reveals substantial temporal and spatial structure. For mid-tropospheric ice clouds, fall streaks with relatively large particle sizes (i.e., colour ratios) are apparent. Of particular interest is that the particles are often larger near cloud bottom, an observation that is established statistically in Sect. 5.3.1. Note that the aerosol event that occurred between 2 and 4 km altitude after 03:00 UTC is largely absent.

Following the example, scattering events from the three winters between 2005 and 2008 were partitioned into four categories based on optical properties and observed structure: aerosols, mixed-phase clouds, ice clouds and boundary-layer ice crystals. "Boundary layer" here refers to the lowest few kilometers of troposphere influenced by the thermal inversion. No distinction is made between a cloud and its precipitate. The categorization was applied using 1 km vertical and 1 h time resolution. Cases with mixtures of different ice crystal types (e.g., precipitation into boundary-layer ice crystals) were removed from the analysis. Mixtures with aerosol particles, however, were included. Aerosol events are very common and, more importantly, the presence of aerosols is difficult to ascertain when other atmospheric phenomena (e.g., blowing snow residuals, ice crystal precipitation) are present. Finally, mixed-phase clouds that were observed to fully glaciate were not re-interpreted as boundary-layer ice crystal events.

The lidar and radar data were filtered to reduce the atmospheric variability and noise within an averaging volume. The lidar data were used to establish the filtering criterion for both instruments given the lidar's higher intrinsic spatial and temporal resolution.

Measurements in an averaging volume with a relative standard deviation in the 532 nm backscatter cross-section greater than 25% were excluded from further analysis.

To facilitate a statistical analysis and interpretation, two-dimensional histograms were produced from both the complete and categorized data sets. All histograms were normalized so that the total probability is one. Histograms with logarithmic horizontal axes have uniform bin sizes in the logarithmic space so that scattering at the full range of available scales is represented.

4 Results

4.1 2005–2008 Data set

Figure 5 shows two-dimensional histograms of occurrence probability against scattering parameters and altitude for the full data set spanning the wintertime months of December through March of 2005 to 2008. 7772 h of measurements over 351 days were used. The distributions contain the signatures of liquid water droplets, aerosols, ice crystals, and particle mixtures. Dissimilar scatterers occupy separate regions in each histogram, as will be shown using the categorized data sets. The full histograms can be used to determine the relative contribution from each scatterer type.

Figure 5a shows the probabilities for depolarization against altitude. There are features in the distribution found below 10% and above 20% linear depolarization, which correspond to predominantly liquid and ice scatterers, respectively. Ice scatterers extend from the ground up to at least 8 km in altitude. Liquid scatterers are mostly found near the ground, except for a small population peaking near 2 km altitude with linear depolarization less than 3%. The near-ground low-depolarization events are associated with aerosols, and the linear depolarizations less than 3% represent droplets in thin water clouds, as will be shown in the sections that follow.

Figure 5b shows the probabilities for colour ratio (a proxy for particle size) against altitude. There is a trend toward smaller particles (i.e., smaller $\beta_{\text{radar}}/\beta_{\text{lidar}}$) with in-

creasing height. Figure 5c shows the probabilities for colour ratio against depolarization. The strong maximum between 15 and 50% linear depolarization is due to ice scatterers, and the low-depolarization "tail" (below 10%) is for mostly liquid scatterers. Notice that ice scatterers (high depolarization) are larger than the liquid scatterers (low depolarization).

Figure 6 shows separate histograms for each category in columns: Aerosols, mixed-phase clouds, ice clouds, and boundary-layer ice crystals. Each category is discussed in respective subsections that follow.

4.2 Aerosols

1199 h of measurements over 103 days were categorized as aerosol scattering. Before analyzing the histograms in Fig. 6, we briefly consider Fig. 7 which provides a histogram for aerosols using all available detections by the lidar. Aerosols are observed to occur mostly below 2 or 3 km in altitude, with depolarization values ranging from 0 to 20 or 30%. The larger depolarization values are due to the presence of ice crystals. Vertical discontinuities in the figure are an artifact of the categorization process, which used 1 km resolution.

Figure 6a provides histograms using the subset of aerosol measurements for which both lidar and radar detections are available. Although aerosols are generally not detected by the radar, the presence of a small quantity of ice crystals can easily elevate the backscatter cross-section above the detection threshold because ice crystals are relatively large and the radar reflectivity is proportional to the sixth power of the particle diameter. Since aerosols are nearly ubiquitous in the Arctic atmosphere, distributions in this column will help to identify aerosol contamination in the ice particle categories.

The top panel of Fig. 6a shows most of the dual lidar-radar aerosol detections occur near ground. This is different from what is seen in Fig. 7, and reflects the fact that ice scatterers are also ubiquitous at the lowest altitudes. Fewer detections were made higher up, and the coarseness of the distribution reflects low-probability statistics. Surface-based aerosols have linear depolarization between 0 and 20%, which is

similar to that seen in Fig. 6. Relatively high depolarizations away from the surface indicate a dominant contribution from ice crystals.

The middle panel of Fig. 6a indicates that aerosol contamination of the other plots in Fig. 6 can be expected primarily at the surface. Similarly, the lower panel indicates that aerosol contamination for depolarizations below 10% and for colour ratios between 10^{-8} and 10^{-7} will be an issue. This corresponds to the "tail" region mentioned in the description of Fig. 5. Note that depolarization values larger than 10% in the bottom panel of Fig. 6a are representative of ice scattering, and so would not be considered a contamination in the other columns.

4.3 Mixed-phase clouds

894 h of measurements over 86 days were used to compile the histograms for mixed-phase clouds shown in Fig. 6b. The distinction between water droplets and ice crystals is evident in the top panel, which shows the depolarization versus altitude. Near-zero values of depolarization extending from 500 m to 3.5 km in altitude are due to droplets in thin water clouds. High linear depolarizations of 20 to 50% are from the frozen condensate, and are found largely below the liquid component heights as would be expected for precipitate. There is a region of intermediate linear depolarization between 3 and 20% which corresponds to the transition region from liquid to ice. The local maximum near ground at 10% depolarization represents a contribution from the aerosols, as established in the top panel of Fig. 6a.

The vertical distribution of probabilities against colour ratio in the middle panel has horizontal streaks for colour ratios between 10^{-9} and 10^{-6} which are from the thin water clouds. The dominant scattering maximum is for ice crystals, which at high colour ratio have much larger sizes than the water droplets. Note that the population has constant colour ratio with height, which indicates uniform size. The bottom panel, which presents the probabilities against the depolarization and colour ratios, confirms the size comparison between the two scatterer types. The water droplet population (linear depolarization <3%) has much smaller colour ratio values compared to the ice

crystal populations (linear depolarization with the greatest part between 20 and 50%). There is a transition region between the two peaks which can be attributed to the phase change from water to ice.

4.4 Ice clouds

1424 h of measurements over 134 days were used to compute the histograms for ice clouds given in Fig. 6c. The top panel shows that linear depolarizations range from about 15 to 45%. The mean linear depolarization decreases with height, from approximately 40% at 2 km to 25% at 5 km altitude. Note that horizontal discontinuities at 1 and 2 km altitude in this panel are an artifact of the selection process resolution described earlier.

In the middle panel, the mean colour ratio decreases with height. This indicates a decrease of mean ice crystal size with height, which is similar to the depolarization trend. Decreasing colour ratio with height is also evident in the example given in Fig. 4. It is interesting to note that small ice particles are evident in approximately equal quantities between 3 and 8 km altitude. A low colour-ratio contribution from aerosols below 1 km is apparent.

The bottom panel gives the probabilities against depolarization and colour ratio. The tail at low depolarization extending from the main population is due to aerosols. Although the upper two panels might suggest that depolarization is a function of particle size, the bottom panel indicates that this is not the case. Small ice crystals tend to have high depolarization (40% – 50%), whereas larger particles span a wide range of depolarization values.

Separate histograms against depolarization and altitude for small and large ice crystal sub-populations are given in Fig. 8. The low-depolarization detections in Fig. 8a represent a contribution from aerosols. The modal depolarization for small ice particles is fairly constant with altitude, although the range of depolarization values become larger with height. This contrasts with large particles that have decreasing depolarization with height (Fig. 8b). The same trend is evident when particles of all sizes are

included (Fig. 6c, top panel). Further comparison of Fig. 8a and b reveals that small ice particles tend to depolarize more than large ones at a given altitude. This result confirms that decreasing depolarization with height cannot be associated with decreasing size.

4.5 Boundary-layer ice crystals

1338 h of measurements over 107 days were used to compute the histograms for boundary layer ice clouds. Results are shown in Fig. 6d. The top panel shows that ice crystals are observed mostly below 750 m altitude. The depolarization spans a large range, including values too low to indicate solid phase. The low-depolarization values are attributed to the presence of aerosols.

The middle panel shows colour ratios that are in the same range as determined for aerosol layers only (Fig. 6a). The calculations were performed again considering data with depolarization values greater than 25% (i.e., ice crystals only), and a very similar plot was obtained. This confirms that the colour ratio values determined for aerosols (Fig. 6a) are biased by the ice crystals contained within. The bottom panel shows that there is no trend in depolarization with colour ratio, except for at very low depolarization where an aerosol tail is apparent.

5 Discussion

5.1 Scattering properties

Comparison of the histograms in Figs. 6 and 7 for the different particle types reveals significant differences in colour ratios, optical properties and vertical distribution. Representative values for each property and particle type are given in Table 4. The values represent estimates corresponding to 10% of the peak level or greater in each histogram. The estimates were obtained visually from each panel because interpretation to account for height variations and interference from aerosols is required.

Water droplets have linear depolarizations less than 3%. Aerosol haze typically has linear depolarization less than 20%, which is different from what is found for liquid droplets alone due to ice content. Ice crystals have linear depolarizations greater than 20%. Water droplets have lower colour ratios than do ice crystals, which indicates the water droplets are smaller. Boundary-layer ice crystals, ice clouds, and ice precipitation from thin water clouds occupy partly overlapping ranges of colour ratio values. Ice crystals precipitating from mixed-phase clouds and lower tropospheric ice clouds generally have greater colour ratios (and therefore sizes) than are observed for boundary-layer ice crystals. Middle tropospheric ice particles have comparable colour ratios to those found in the boundary layer.

Ice clouds have depolarization decreasing with altitude (Fig. 6c, top panel). This trend is associated with large particles (Fig. 8b), and contrasts with the nearly constant modal depolarization for small particles (Fig. 8a). The measurements indicate that the large-particle morphology changes with altitude, perhaps in response to particle breaking or sublimation (see, for example, Whiteway et al. (2004). Small particles have greater depolarization than large particles, for unknown reasons. In situ sampling would help provide further insight into the depolarization problem.

5.2 Mie theory computations of particle effective radius

Mie scattering theory can be used to convert colour ratio to spherical particle effective radius r_{eff} defined by

$$r_{\text{eff}} = \frac{\int_0^\infty n(r) r^3 dr}{\int_0^\infty n(r) r^2 dr}$$

where r is the radius, and $n(r)$ is the number density. The interpretation of effective radius in terms of actual particle dimensions will be discussed shortly. We employed the algorithms from Mishchenko et al. (2002) to determine mean particle backscatter cross-sections $\overline{\sigma}_\pi$ for distributions of spherical particles characterized by r_{eff} and

effective variance v_{eff} given by

$$v_{\text{eff}} = \frac{\int_0^\infty n(r)(r - r_{\text{eff}})^2 r^2 dr}{r_{\text{eff}}^2 \int_0^\infty n(r) r^2 dr} \quad .$$

The effective radius and variance are used in our analysis because the results for colour ratio are relatively insensitive to the specific distribution of particles used. For example, although our calculations have assumed a gamma distribution of particles, we have verified that a modified power-law distribution with the same parameters produces similar results.

The parameters required for the Mie calculations include the particle refractive index and the wavelength of the incident light. Table 5 gives the choices used in this study. The refractive index n_i is wavelength dependent, and in the case of radar waves has a large imaginary part for water droplets which implies a strong absorption component.

Figure 9 presents the results of the Mie computations. Curves are given for ice and water particles for a selection of v_{eff} values. The plot allows conversion of colour ratios to effective radii ranging from 1 to more than 100 microns once a choice of particle type and v_{eff} is made.

Colour ratio values in Table 4 were converted to effective radius using the Mie computations for v_{eff}=0.1. This choice of effective variance is relatively narrow and produces colour ratio curves that smoothly interpolate those obtained with monodisperse distributions. The choice of narrow distributions is appropriate given the high spatial and temporal resolutions in use, and the corresponding high degree of variability revealed in the colour ratios of Fig. 4. In the case that the actual distributions have greater effective variance, say 0.3, the maximum systematic error expected in our effective radius estimates is less than +25%.

Computations may also be performed for non-spherical particles, but were not pursued here because we have no information on particle habit. Depolarization cannot be used as an unambiguous detector of ice particle shape, and so the incorporation of depolarization into the present analysis is not possible. Furthermore, the range of particle morphologies in ice clouds is very broad (Whiteway et al., 2004), and so choosing any one particle type is arbitrary.

Instead, we focus on the interpretation of effective radius measurements in terms of observed particle shapes. Mahesh et al. (2001) demonstrated that effective radii determined from infrared remote sensing agree with radii for equivalent volume-to-area (V/A) spheres from sampled ice crystals. In a series of papers, Grenfell et al. (1999), Neshyba et al. (2003) and Grenfell et al. (2005) showed that the equal-V/A sphere diameter is characteristic of the smallest dimension for a variety of realistic particle types. For example, the equal-V/A diameter is comparable to a column particle's width rather than its length. They also argued that the equal-V/A radius is of high importance for radiative transfer. In the comparisons that follow, we will therefore consider our effective radius determination to be associated with the smallest particle dimension.

Our approach differs from some others found in the literature. More complicated methods are necessary when the visible backscatter cross-section is not directly measured (see Donovan et al., 2001, for example), but is not needed when high spectral resolution lidar is used. Alternative derivations of particle sizes can be made in terms of cloud extinction using the Raman lidar technique (e.g., Wang and Sassen, 2002), but much longer integrations are required to achieve an appropriate signal-to-noise level, and so they are not of interest here.

5.3 Comparisons with other measurements

5.3.1 Particle effective radii

Comparison of our measurements with values from the literature is complicated by differences in the measurement techniques. We have provided histograms of occurrence probability for effective radii measured at high spatial and temporal resolution, whereas in-situ measurements typically provide distributions of number concentration against particle size averaged over a long period of time or distance. However, if our assumption of narrow particle size distributions in each measurement volume is correct, a

comparison of effective radii measured using the radar and lidar against the range of particle sizes observed with in-situ techniques is appropriate. Where possible, comparisons are made with the smallest dimension of the sampled particles, which is the approach proposed in Sect. 5.2.

For mixed-phase clouds, Arctic aircraft measurements by Curry et al. (2000) show water droplet sizes that range from about 2 to 47 µm. Frozen precipitation below the liquid stratus ranges from a few tens to several hundred microns in length (widths were not given). Although the measurements were taken during summer and in the vicinity of Barrow, Alaska (71° N) which is further south than Eureka (80° N), their results are in reasonable agreement with our values of 5 to 40 µm and 40 to 220 µm, respectively. The smaller maximum size we measured for ice crystals can be attributed to the sensitivity of our technique to particle widths rather than lengths.

Comparison data for the ice cloud measurements are difficult to find. Wintertime in-situ aircraft campaign data are not available, presumably due to the difficulties of flying experiments in dark conditions. Summertime clouds in the middle troposphere are often of the mixed-phase variety, and are observed in much warmer conditions. High altitude in-situ cirrus measurements in the Arctic are not available.

Lawson et al. (2001) show one case of a mid-tropospheric cirrus cloud sampled at Barrow Alaska on 29 July 1998 during FIRE ACE. They reported that small particles were found in clumps with very high local concentrations that are interspersed with regions of larger particles in low concentrations. This is consistent with the structured ice clouds seen at Eureka and illustrated by the example in Fig. 4. Their in-situ measurements revealed particles ranging from less than 10 to hundreds of microns, which is consistent with our measured values of 25 to 220 µm.

A comparison can also be made with mid-latitude cirrus, which are observed at temperatures similar to the wintertime Arctic mid-troposphere. Aircraft sampling of mid-latitude cirrus by Whiteway et al. (2004) revealed particle sizes ranging from less than 10 to a few hundred microns. Radar/lidar inversions by Donovan and van Lammeren (2002) also yield effective particle sizes up to a few hundred microns in radius. They

showed that mid-latitude cirrus have effective radius increasing with increasing temperature, which is consistent with our observations of decreasing size with increasing height. Whiteway et al. (2004) showed that particle size variations with height are determined by a competition between the growth and sedimentation of large particles with crystal breakage into smaller particles and evaporation. The preponderance of larger crystals at low altitudes in our observations is therefore likely due to growth and/or sedimentation.

In-situ measurements of ice crystal sizes for residual blowing snow particles lofted from mountainous terrain into the boundary layer are not available for the High Arctic. Measurements at the South Pole station during winter show residual blowing snow crystals from 2 to 28 µm in radius (Walden et al., 2003). These are somewhat smaller than the 15 to 70 µm that we have observed, which is likely due to the colder Antarctic conditions (Lesins et al., 2009a).

The fact that comparisons of our data with results in the literature has been successful is a partial validation of the measurement technique and lends confidence to the ensuing results. However, a formal validation of the remote-sensing measurements with local aircraft measurements during winter would be very useful and would fill an important gap left by Arctic aircraft measurement programs.

5.3.2 Ice Crystal Altitudes

Boundary-layer ice crystals are found predominantly below 750 m altitude, which comparable to the height of the mountain ridges near Eureka. Lesins et al. (2009a) showed four case studies of topographic blowing snow residuals that share the same vertical distribution. This indicates that blowing snow residuals are the dominant contributor to high optical depth boundary-layer ice crystal populations at Eureka. This result likely extends to other locations in the rugged High Arctic.

Ice clouds are observed throughout the troposphere during winter. At times these ice clouds, which are generated in the same range of temperatures as cirrus clouds at mid-latitudes, can precipitate to the ground. Future studies might take this into account

for particle sampling when aircraft are not available.

The altitude range for thin water stratus (0.5–3.5 km) is smaller than is observed during other seasons (e.g., Curry et al., 1996). The wintertime range corresponds with the observed variability for wintertime surface thermal inversion layer depths given by Lesins et al. (2009b). This suggests that thin liquid water stratus are connected to the development of wintertime surface inversion layers.

It has been known since Wexler (1936) that cold surface temperatures in the Arctic winter are due to radiative cooling by surface snow and ice. More advanced models of the radiative transfer process (e.g., Curry, 1983) showed that in clear air the surface temperatures should be much lower than is observed, which suggests an important role for particles in determining boundary layer temperatures. Curry (1983) proposed a variety of mechanisms that could contribute to the process. These included the radiative impact of diamond dust and liquid condensate, and mixing by turbulence. A role for diamond dust has been discounted by the measurements of Intrieri and Shupe (2004) and Lesins et al. (2009a), and a role for turbulence has yet to be experimentally investigated. Our measurements support the contention of Intrieri and Shupe (2004) that liquid condensate plays an important role. Although the model of Curry (1983) did not produce the kind of thin liquid water clouds discussed here, the water clouds it simulated suggested the same basic mechanism. Thin water cloud dynamics and microphysics are further explored by Shupe et al. (2008).

5.3.3 Depolarization

The depolarization of aerosol layers is greater than what is found for liquid droplets. Hoff (1988) showed that ice crystals are responsible for the elevated depolarizations in Arctic haze, and we make the same interpretation here.

Figure 8 established that the depolarization of small particles in ice clouds was greater than for large particles at a given altitude. High depolarization in contrails, which also contain very small particles, was found by Sassen (1997). Young cirrus were shown to have linear depolarization values in excess of 50%. The reasons for

this result was unknown to Sassen (1997), as is the case here. Further investigation is required to understand the nature of small particle scatterers in ice clouds.

5.4 Classification chart

The histograms of Fig. 6 reveal that different scatterer types occupy different regions in particle size-depolarization space. Figure 10 provides a classification chart from the compiled information. The thresholds are approximate, and lead to relatively large regions occupied by particle mixtures. Note that areas with only aerosol particles cannot be interpreted in terms of size or colour ratio because the radar's sensitivity is too low to detect such small particles.

The lidar volume backscatter cross-section can be used to isolate locations where aerosol layers dominate. The range in lidar volume backscatter cross-section for aerosols is relatively narrow, indicating that variations in sizes and number densities are small. Lidar backscatter cross-sections β_{lidar} that are smaller than 2×10^{-5} m^{-1} sr^{-1} are characteristic of aerosol layers and this threshold can be used to distinguish aerosol layers from the mixtures.

In Fig. 10, mixed-phase cloud ice precipitation and boundary-layer ice crystals occupy distinct regions. Ice clouds, however, overlap with both. Some differentiation can be made on the basis of altitude, as shown in Table 4: small ice crystals below 2 km altitude are generally classified as boundary-layer ice particles, whereas small ice crystals in ice clouds are found predominantly higher up. Ice crystals originating from mixed-phase clouds and ice clouds are indistinguishable on this basis.

6 Conclusions

A combined radar-lidar technique was used to study particle properties in the High Arctic troposphere during winter. Different particle types were compared in terms of depolarization, colour ratio, and vertical distribution. The colour ratio is independent of

particle number density and therefore related to particle size. Colour ratios cannot be determined for aerosols because they are not detected by the radar, except in mixtures.

Particle effective radii determined using Mie scattering theory are consistent with others found in the literature. Water droplets are small (effective radii of a few tens of microns) while ice particles can be much larger (effective radii up to a few hundred microns). In the boundary layer, mixed-phase precipitate provides the largest ice crystals whereas residual blowing snow particles lofted from mountain ridges are smallest. Ice cloud particles span the full range of ice crystal sizes, and have a strong gradient in with altitude with the largest particles at the lowest heights. Small ice cloud particles are distributed reasonably uniformly above 3 km altitude.

Depolarization is highly dependent on the particle type. Particle scattering dominated by aerosols has linear depolarization less than 20%, whereas ice crystals scattering has linear depolarization greater than 20%. Much of the depolarization in aerosol layers likely originates from ice crystals mixed in. Water droplets, in contrast, have linear depolarizations less than 3%. Ice clouds in the middle troposphere have depolarization decreasing with altitude, and this trend is reflected in the large particle sub-population. Small particles in ice clouds have greater depolarization than large ones at any given altitude, and almost constant modal depolarization with height. The measurements indicate that particle morphology changes with altitude.

Thin water layers associated with mixed-phase clouds are observed from 500 m to 3.5 km altitude, which is the same range as is seen for thermal inversion layer depths (Lesins et al., 2009b). This correlation suggests that mixed-phase clouds are connected to the development of wintertime thermal inversion layers.

A classification chart was produced which allows for the identification of ice crystals, aerosols and water droplets from a combination of depolarization and colour ratio values. The chart allows a deeper understanding of the particles found above Eureka's by associating them with a shape and size-related parameter.

Future efforts are needed to improve our understanding of particle microphysics and optical properties. In situ measurements of particle morphologies are required to understand the relationship between size, shape and depolarization. This may be partly possible from ground level since each ice crystal type is observed to precipitate to the surface. The addition of data from other instruments located at ØPAL may be used to improve particle size retrievals, especially for aerosols which are not detected by the radar. Profile measurements of temperatures and water vapour could provide insight into the formation and maintenance processes of the different atmospheric particles. Such measurements will be available in the near future from the CANDAC Raman Lidar.

Acknowledgements. Financial support for this research was provided by the Canadian Foundation for Climate and Atmospheric Research (CFCAS), the Canadian Foundation for Innovation (CFI), the National Science and Engineering Research Council (NSERC) of Canada, the Canadian Space Agency (CSA), the Ontario Innovation Trust (OIT), the Ontario Research Fund (ORF), the Nova Scotia Research and Innovation Trust (NSRIT), the Government of Canada International Polar Year fund, and NSF grant ARC-0612452 and NOAA contract RA133R07CN0281. Logistical and other in-kind support from Environment Canada, the staff of the Eureka Weather Station, the PEARL Manager Pierre Fogal and Operators Alexei Khmel, Paul Loewen, Oleg Mikhailov, Ashley Harrett and Matthew Okraszewski is gratefully acknowledged.

References

Blanchet, J.-P. and Girard, E.: Water vapor-temperature feedback in the formation of continental Arctic air: its implication for climate, Sci. Total Environ., 160/262, 793–802, 1995. 7783

Curry, J.: On the formation of continental polar air, J. Geophys. Res., 40, 2278–2292, 1983. 7782, 7801

Curry, J. A., Schramm, J. L., and Ebert, E. E.: Impact of clouds on the surface radiation balance of the Arctic Ocean, Meteorol. Atmos. Phys., 51, 197–217, 1993. 7783

Curry, J. A., Rossow, W. B., Randall, D., and Schramm, J. L.: Overview of Arctic cloud and radiation characteristics, J. Climate, 9, 1731–1764, 1996. 7782, 7783, 7801

Curry, J. A., Hobbs, P. V., King, M. D., Randall, D. A., Minnis, P., Isaac, G. A., Pinto, J. O., Uttal, T., Bucholtz, A., Cripe, D. G., Gerber, H., Fairall, C. W., Garrett, T. J., Hudson, J., Intrieri, J.

M., Jakob, C., Jensen, T., Lawson, P., Marcotte, D., Nguyen, L., Pilewskie, P., Rangno, A., Rogers, D. C., Strawbridge, K. B., Valero, F. P. J., Williams, A. G., and Wylie, D.: FIRE Arctic Clouds Experiment, B. Am. Meteor. Soc., 81, 5–29, 2000. 7783, 7784, 7799

Donovan, D. P. and van Lammeren, A. C. A. P.: Cloud effective particle size and water content profile retrievals using combined lidar and radar observations 1. Theory and examples, J. Geophys. Res., 106, 27425–27448, 2001. 7798

Donovan, D. P. and van Lammeren, A. C. A. P.: First ice cloud effective particle size parameterization based on combined lidar and radar data, Geophys. Res. Lett., 29(1), 1006, doi:10.1029/2001GL013731, 2002. 7799

Grenier, P., Blanchet, J.-P., and Munoz-Alpizar, R.: Study of Polar Thin Ice Clouds and Aerosols Seen By CLOUDSAT and CALIPSO During Mid-Winter 2007, J. Geophys. Res., doi:10.1029/2008JD010927, in press, 2009. 7790

Grenfell, T. C. and Warren, S. G.: Representation of a nonspherical ice particle by a collection of independent spheres for scattering and absorption of radiation, J. Geophys. Res., 104, 31697–31709, 1999. 7798

Grenfell, T. C., Neshyba, S. P., and Warren, S. G.: Representation of a nonspherical ice particle by a collection of independent spheres for scattering and absorption of radiation: 3. Hollow columns and plates, J. Geophys. Res., 110, D17203, doi:10.1029/2005JD005811, 2005. 7798

Hoff, R. M.: Vertical structure of Arctic haze observed by lidar, J. Appl. Meteor., 27, 125–139, 1988. 7783, 7801

Intrieri, J. M. and Shupe, M. D.: Characteristics and radiative effects of diamond dust over the Western Arctic Ocean region, J. Climate, 17, 2953–2960, 2004. 7783, 7786, 7801

Lesins, G., Bourdages, L., Duck, T. J., Drummond, J. R., Eloranta, E. W., and Walden, V. P.: Large surface radiative forcing from topographic blowing snow residuals measured in the High Arctic at Eureka, Atmos. Chem. Phys., 9, 1847–1862, 2009, http://www.atmos-chem-phys.net/9/1847/2009/. 7783, 7800, 7801

Lesins, G., Duck, T. J., and Drummond, J. R., Climatology of Eureka in the Canadian High Arctic, Atmos.-Ocean., in preparation, 2009. 7782, 7801, 7803

Lawson, R. P., Baker, B. A., and Schmitt, C. G.: An overview of microphysical properties of Arctic clouds observed in May and July 1998 during FIRE ACE, J. Geophys. Res., 106, 14989–15014, 2001. 7799

Leaitch, W. R., Hoff, R. M., and MacPherson, J. I.: Airborne and lidar measurements of aerosol

and cloud particles in the troposphere over Alert Canada in April 1986, J. Atmos. Chem., 9, 187–211, 1989. 7783, 7789

Mahesh, A., Walden, V. P., and Warren, S. G.: Ground-based infrared remote sensing of cloud properties over the Antarctic Plateau. Part II: Cloud optical depths and particle sizes, J. Appl. Meteorol., 40, 1279–1294, 2001. 7798

Moran, K., Martner, B., Post, M., Kropfli, R., Welsh, D., and Widener, K.: An unattended cloud-profiling radar for use in climate research, B. Am. Meteor. Soc., 79, 443–355, 1998. 7787

Mishchenko, M. L., Travis, L. D., and Lacis, A. A.: Scattering, absorption, and emission of light by small particles, Cambridge University Press, ISBN 0-521-78252-X, 448 pp., 2002. 7796

Neshyba, S. P., Grenfell, T. C., and Warren, S. G.: Representation of a nonspherical ice particle by a collection of independent spheres for scattering and absorption of radiation: 2. Hexagonal columns and plates, J. Geophys. Res, 108(D15), 4448, doi:10.1029/2002JD003302, 2003. 7798

Razenkov, I., Eloranta, E., Hedrick, J., Holz, R., Kuehn, R., and Garcia, J.: A high spectral resolution lidar designed for unattended operation in the Arctic, in: Lidar Remote Sensing in Atmospheric and Earth Sciences, edited by: Bissonnette, L. R., Roy, G., and Vallee, G., 57–60, Defence R&D Canada-Valcartier, Val-Belair, Quebec, Canada, 2002. 7786

Sassen, K.: Contrail-Cirrus and Their Potential for Regional Climate Change, B. Am. Meteor. Soc., 78, 1885–1903, 1997. 7801, 7802

Shupe, M. D., Kollias, P., Persson, P. O. G., and McFarquhar, G. M.: Vertical motions in Arctic mixed-phase stratiform clouds, J. Atmos. Sci., 65(4), 1304–1322, doi:10.1175/2007JAS2479.1, 2008. 7801

Trivett, N. B. A., Barrie, L. A., Bottenheim, J. W., Blanchet, J.-P., den Hartog, G., Hoff, R. M., and Mickle, R. E.: An experimental investigation of Arctic haze at Alert, N. W. T., March 1985, Atmos. Ocean., 26, 341–376, 1988. 7783

Uttal, T., Curry, J. A., McPhee, M. G., Perovich, D. K., Moritz, R. E., Maslanik, J. A., Guest, P. S., Stern, H. L., Moore, J. A., Turenne, R., Heiberg, A., Serreze, M. C., Wylie, D. P., Persson, O. G., Paulson, C. A., Halle, C., Morison, J. H., Wheeler, P. A., Makshtas, A., Welch, H., Shupe, M. D., Intrieri, J. M., Stamnes, K., Lindsey, R. W., Pinkel, R., Pegau, W. S., Stanton, T. P., and Grenfeld, T. C.: Surface Heat Budget of the Arctic Ocean, B. Am. Meteor. Soc., 83, 255–275, 2002. 7783

Verlinde, J., Harrington, J. Y., McFarquhar, G. M., Yannuzzi, V. T., Avramov, A., Greenberg, S., Johnson, N., Zhang, G., Poellot, M. R., Mather, J. H., Turner, D. D., Eloranta, E. W., Zak, B.

D., Prenni, A. J., Daniel, J. S., Kok, G. L., Tobin, D. C., Holz, R., Sassen, K., Spangenberg, D., Minnis, P., Tooman, T. P., Ivey, M. D., Richardson, S. J., Bahrmann, C. P., Shupe, M., DeMott, P. J., Heymsfield, A. J., and Schofield, R.: The mixed-phase Arctic cloud experiment, B. Am. Meteor. Soc., 80, 205–221, 2007. 7783

Walden, V. P., Warren, S. G., and Tuttle, E.: Atmospheric ice crystals over the Antarctic Plateau in winter, J. Appl. Meteorol., 42, 1391–1405, 2003. 7800

Wang, Z. and Sassen, K.: Cirrus cloud microphysical property retrieval using lidar and radar measurements. Part I: Algorithm description and comparison with in situ data, J. Appl. Meteorol., 41, 218–229, 2002. 7798

Warren, S. G. and Brandt, R. E.: Optical constants of ice from the ultraviolet to the microwave: A revised compilation, J. Geophys. Res., 113, D14220, doi:10.1029/2007JD009744, 2008. 7812

Wexler, H.: Cooling in the lower atmosphere and the structure of polar continental air, Mon. Weather Rev., 64, 122–136, 1936. 7801

Whiteway, J. A., Cook, C., Gallagher, M., Choularton, T., Harries, J., Connolly, P., Busen, R., Bower, K., Flynn, M., May, P., Aspey, R., and Hacker, J.: Anatomy of cirrus clouds: Results from the Emerald airborne campaigns, Geophys. Res. Lett., 31, L24102, doi:10.1029/2004GL021201, 2004. 7796, 7798, 7799, 7800

Table 1. Instrument complement and measurement capabilities at ØPAL.

Instrument	Measurements
Arctic High Spectral Resolution lidar (AHSRL)	Particle optical properties including depolarization
Millimeter-wave Cloud Radar (MMCR)	Cloud reflectivity and Doppler velocity
Atmospheric Emitted Radiance Interferometer (AERI)	Zenith infrared spectral radiances
CANDAC Raman Lidar (CRL)	Particle optical properties, temperatures and water vapor
Tropospheric Ozone Lidar	Ozone concentration
Microwave Radiometer	Water vapor column
CIMEL Sun photometer	Aerosol optical depth and column size distribution
Star photometer	Aerosol optical depth

Table 2. AHSRL specifications.

Transmitter	
Type	Diode-pumped seeded Nd:YAG laser
Wavelength	532 nm
Avg. power	200 mW
Spectral width	<1 pm
Rep. Rate	4 kHz
Beam diameter	0.4 m
Receiver	
Field of view	45 µrad
Spectral bandpass	8 GHz pressure tuned etalon
Aperture	0.4 m
Data acquisition	Photon counting
Detectors	Geiger-mode APDs
Spatial resolution	7.5 m
Temporal resolution	2.5 s
Range	75–30 000 m

Table 3. Millimeter-wave Cloud Radar (MMCR) specifications

Transmitter	
Type	Travelling wave tube
Lifetime	>20 000 h
Wavelength	8.6 mm (Frequency=34.86 GHz)
Avg. power	up to 25 W
Beam width	0.3°
Receiver	
Type	Tilted flat radome Antenna
Diameter	1.8 m
Sensitivity	approx. −40 dBZ at 10 km
Spatial resolution	90 m
Temporal resolution	10 s
Range	90–20 000 m

Table 4. Ranges for linear depolarization δ_{lin}, colour ratio, effective radius r_{eff} and altitudes z for aerosols, mixed-phase (M-P) cloud water droplets (WD) and ice crystals (IC), ice cloud ice crystals, and boundary-layer (B-L) ice crystals. The ice crystal and water droplet values are from Fig. 6 and the aerosol values are from Fig. 7.

Particle	δ_{lin} (%)	colour ratio	r_{eff} (µm)	z (km)
Aerosols	<20			<3 km
M-P Cloud WD	<3	10^{-9}–10^{-6}	5–40	0.5–3.5
M-P Cloud IC	20–50	10^{-6}–10^{-3}	40–220	0–3
Ice Cloud IC	20–50	10^{-7}–10^{-4}	25–120	>3.5
		10^{-6}–10^{-3}	40–220	<3.5
B-L IC	>20	10^{-8}–10^{-5}	15–70	<0.7

Table 5. Values for wavelengths (λ) and complex refractive indices (n_i) used in the Mie scattering computations for the lidar and radar. Refractive indices are from Warren and Brandt (2008).

	Lidar	Radar
λ	532 nm	8.6 mm
n_i(ice)	1.31	1.8+0.0003i
n_i(water)	1.33	5+2.5i

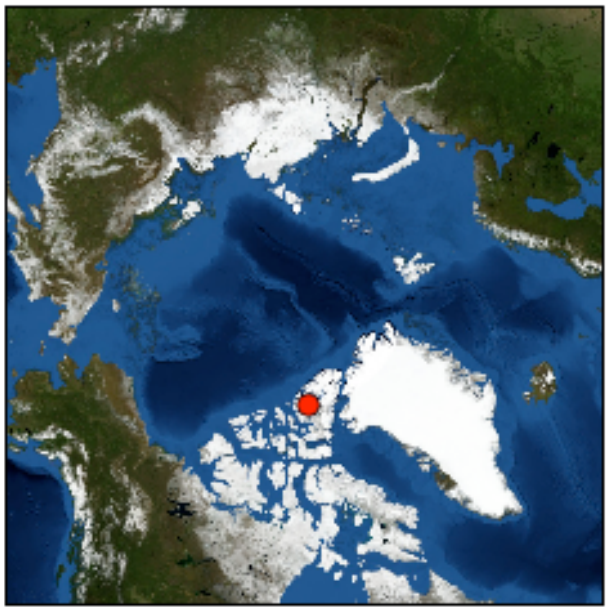

Fig. 1. Polar map of the Arctic. The location of Eureka (80° N, 86° W) is marked with a red dot.

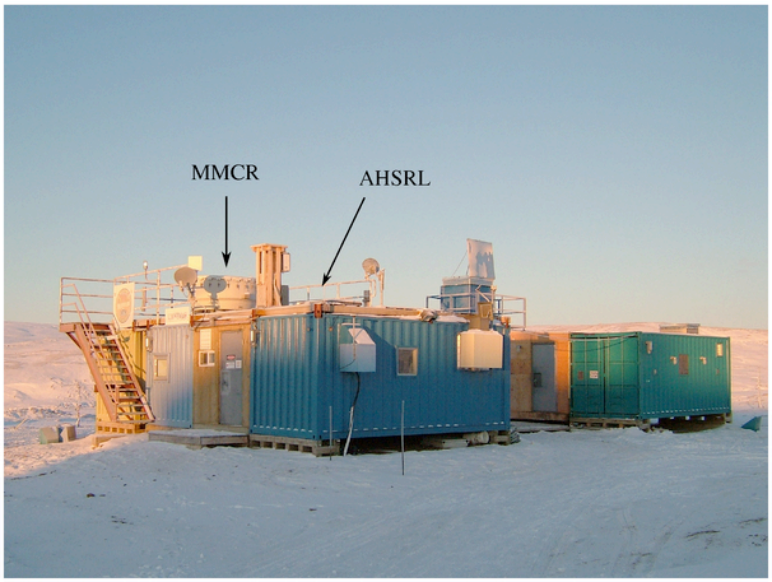

Fig. 2. A photograph of the Zero-altitude PEARL Auxiliary Laboratory (ØPAL) with pointers to the Arctic High Spectral Resolution Lidar (AHSRL) and Millimeter-wave Cloud Radar (MMCR) locations.

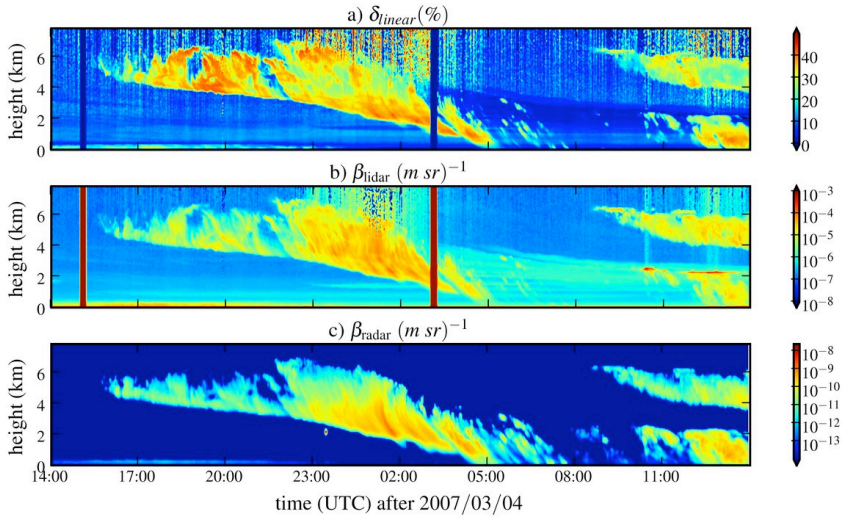

Fig. 3. Example of time series from 4 to 5 March 2007 of **(a)** depolarization, **(b)** lidar volume backscatter cross-section, and **(c)** radar backscatter cross-section.

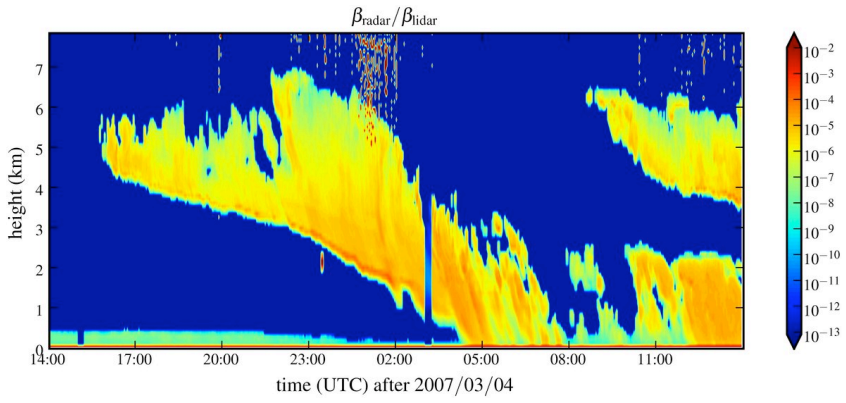

Fig. 4. The colour ratio ($\beta_{\text{radar}}/\beta_{\text{lidar}}$) for the measurement in Fig. 3.

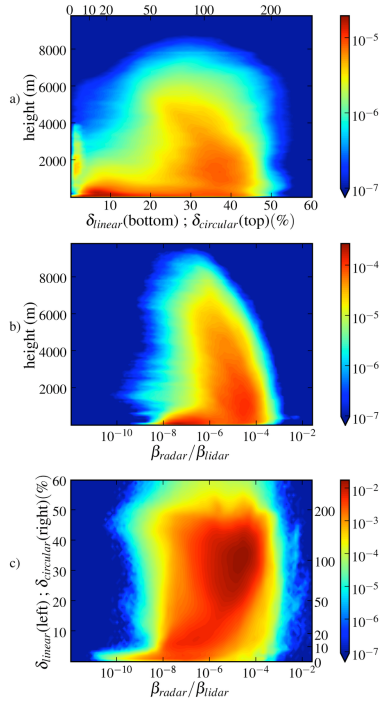

Fig. 5. Average occurrence probability histograms during winter (2005–2008) for **(a)** the vertical distribution of depolarization, **(b)** the vertical distribution of the colour ratio, and **(c)** the colour ratio and depolarization. Detections by both lidar and radar were required.

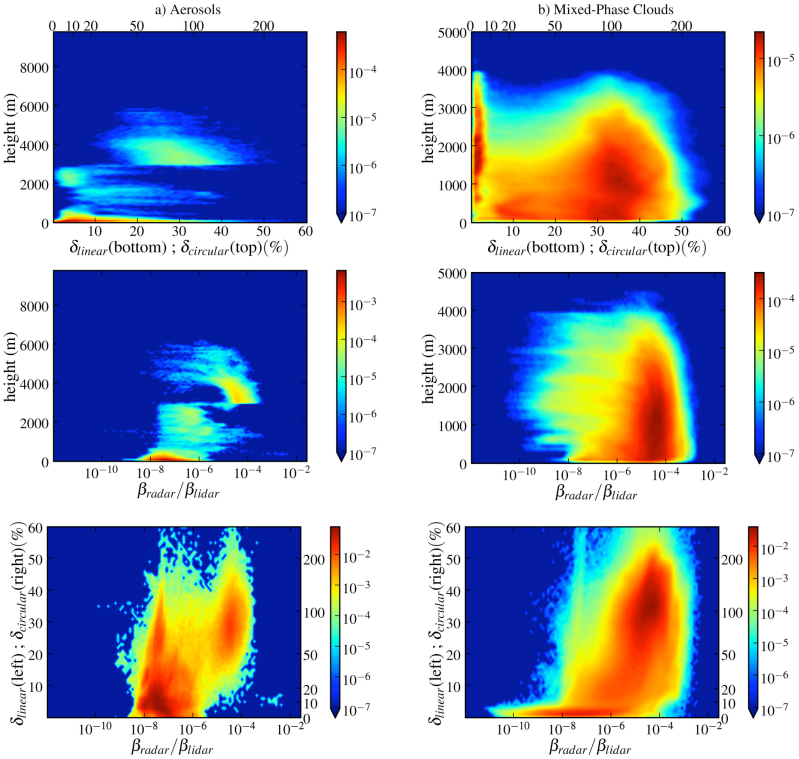

Fig. 6. Occurrence probability histograms arranged in columns for **(a)** aerosols, **(b)** mixed-phase clouds, **(c)** ice clouds, and **(d)** boundary-layer ice crystals. Detections by both lidar and radar were required.

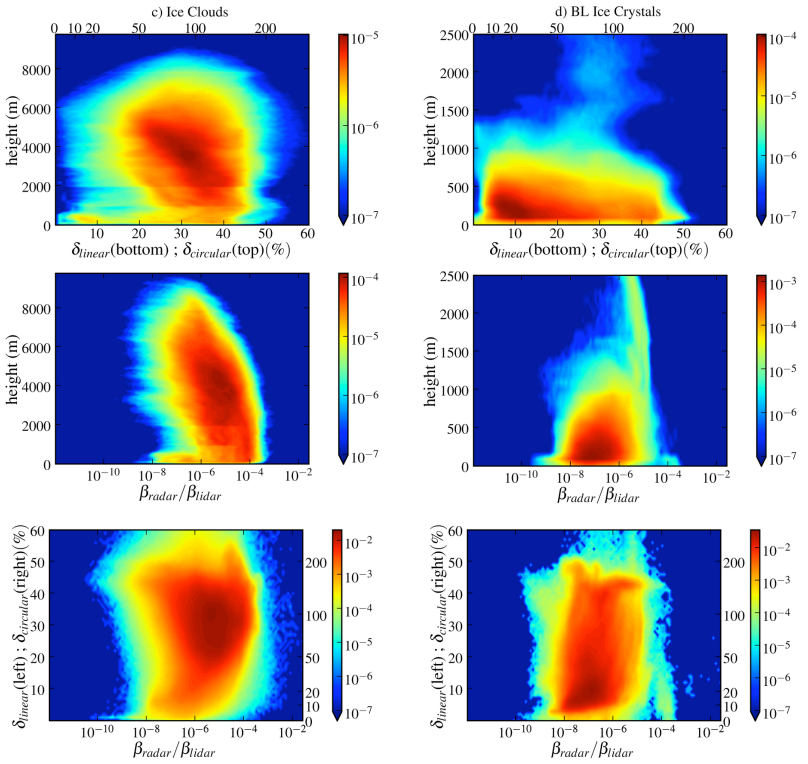

Fig. 6. Continued.

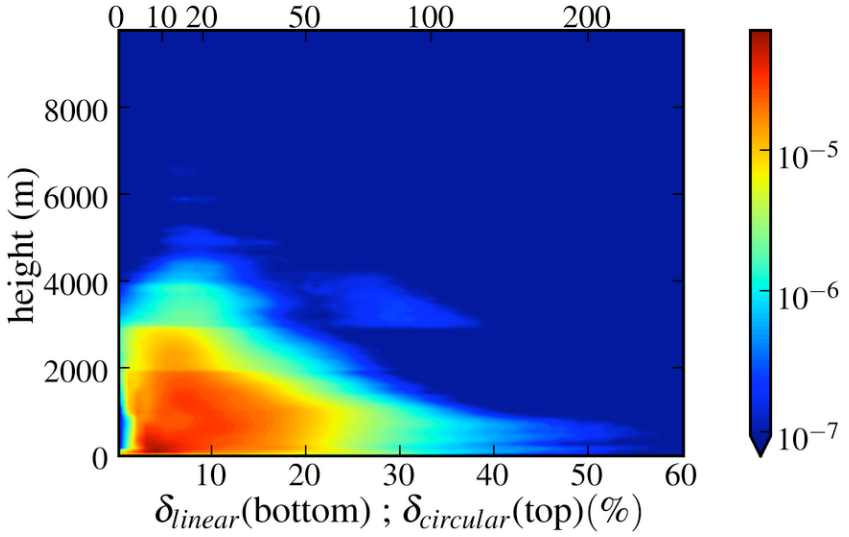

Fig. 7. Occurrence probability histogram for aerosols against height and depolarization, using all available lidar detections.

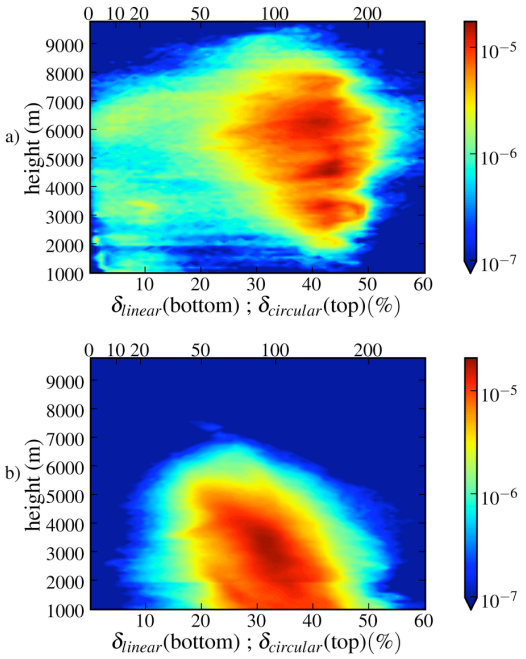

Fig. 8. Occurrence probability histograms for ice clouds against altitude and depolarization for **(a)** small particles (colour ratios $<10^{-7}$), and **(b)** large particles (colour ratios $>10^{-5}$).

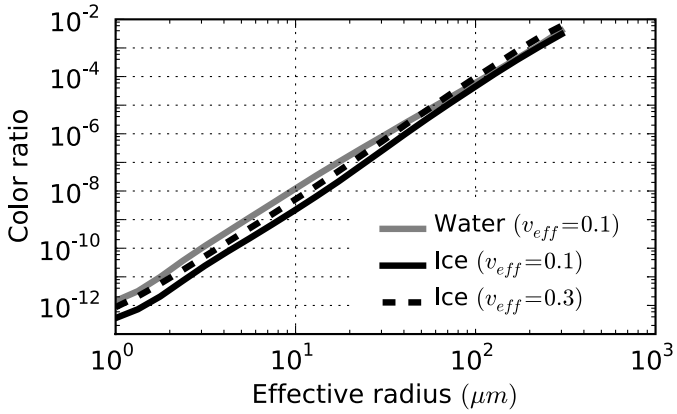

Fig. 9. The relationship between effective radius and colour ratio determined using Mie scattering theory for ice and water spheres.

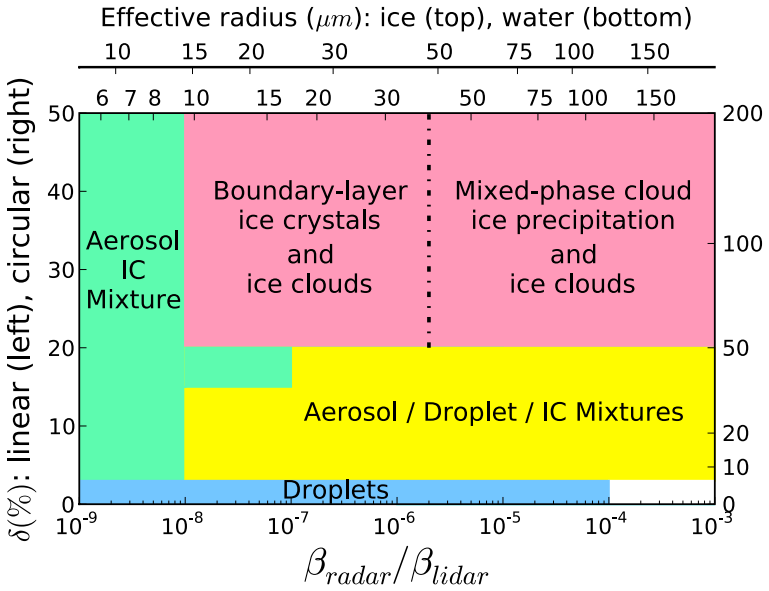

Fig. 10. Classification chart for the different atmospheric particles and their mixtures. The vertical axis shows the linear (left) and circular (right) depolarizations and the horizontal axis is in terms of the color ratio $\beta_{radar}/\beta_{lidar}$ (bottom) and the particle effective radius (top) for ice crystals (IC) and water droplets separately. Effective radii can only be attributed to regions with no aerosol content. The dash-dot line separates the boundary layer ice crystals on the left and precipitation from thin water clouds on the right. Ice clouds span the full region for ice crystals.